Available online at www.sciencedirect.com

ScienceDirect

Ceramics International 40 (2014) 2707–2715

CERAMICS INTERNATIONAL

www.elsevier.com/locate/ceramint

Sol–gel derived amorphous/nanocrystalline MgZnO thin films annealed by atmospheric pressure plasma jets

Shao-Tzu Lien[a], Jian-Zhang Chen[a,*], Yao-Jhen Yang[b], Cheng-Che Hsu[b], I-Chun Cheng[c,d]

[a]*Graduate Institute of Applied Mechanics, National Taiwan University, No. 1, Sec. 4, Roosevelt Rd., Taipei City 10617, Taiwan*
[b]*Department of Chemical Engineering, National Taiwan University, Taipei City 10617, Taiwan*
[c]*Graduate Institute of Photonics and Optoelectronics, National Taiwan University, Taipei City 10617, Taiwan*
[d]*Department of Electrical Engineering, National Taiwan University, Taipei City 10617, Taiwan*

Received 9 September 2013; received in revised form 11 October 2013; accepted 11 October 2013
Available online 23 October 2013

Abstract

This paper reports the characterization of sol–gel derived MgZnO thin films annealed by atmospheric pressure plasma jets (APPJs). $Mg_xZn_{1-x}O$ films exhibit high transparency (> 80%) in the visible light wavelength region. When 20 at% Mg is incorporated into the film, the optical bandgap reveals a blue shift from ~3.25 to ~3.5 eV and the resistivity increases by three to four orders of magnitude, owing to the substitution of Mg atoms into the Zn lattice sites. The absorption band edge becomes sharper and the bandgap becomes slightly narrower as the APPJ treatment time increases. This can be attributed to slight grain growth in the films. When the material is amorphous/nanocrystalline, the quantum confinement effect causes a slight decrease in the bandgap as the grain size increases, resulting in slope alteration at the absorption edge. Compressive stresses caused by the difference in the thermal expansion coefficients between the film and the substrate are generated during the drying process. This leads to surface wrinkling on the sol–gel derived $Mg_{0.2}Zn_{0.8}O$ thin films.

Keywords: D. ZnO; Annealing; Atmospheric pressure plasma jet; MgZnO; Sol–gel

1. Introduction

ZnO is a promising candidate material for short-wavelength optoelectronic devices owing to its wide bandgap (≈ 3.37 eV) and large exciton binding energy (≈ 60 meV) at room temperature [1]. ZnO-based materials have been applied to various types of optoelectronic devices such as gas sensors [2,3], thin-film transistors [4–8], pn diodes [9,10], LEDs [11], UV detectors [12–16], and solar cells [17]. To modulate the bandgap, ZnO can be alloyed with MgO to form $Mg_xZn_{1-x}O$ [18–22]. It has been demonstrated that the bandgap of $Mg_xZn_{1-x}O$ increases from 3.37 to 3.99 eV when the Mg concentration is increased up to x=0.33 [20]. Similar bandgap modulation has been found in Mg alloyed InZnO material systems [23,24]. Because the ionic radii of Mg^{2+} and Zn^{2+} are similar, Zn can be substituted by Mg without much lattice distortion [20]. $Mg_xZn_{1-x}O$ can also be used with ZnO to form $Mg_xZn_{1-x}O$/ZnO heterostructures in which the polarization field at the interface can induce two-dimensional electron gases [25–33].

Several fabrication processes have been developed for $Mg_xZn_{1-x}O$ thin films. Molecular beam epitaxy (MBE) [34,35], pulse laser deposition (PLD) [36,37], metal-organic chemical vapor deposition (MOCVD) [38,39], and atomic layer deposition (ALD) [22] are frequently used for fabricating high-quality $Mg_xZn_{1-x}O$ films. However, with regard to large-area electronics, low cost large-area compatible deposition processes such as sputtering [19,40], sol–gel [41–43], and spray pyrolysis [44,45] are desired fabrication technologies. In this paper, we report the characterization of sol–gel derived $Mg_xZn_{1-x}O$ thin films annealed by atmospheric pressure plasma jets (APPJs). APPJs consist highly energetic N_2 molecules in the plasma jets that provide additional energy to assist the annealing process, which can shorten the processing time [29,46]. When oxygen is involved in APPJs, both the

*Corresponding author. Tel./fax: +886 2 3366 5694.
E-mail address: jchen@ntu.edu.tw (J.-Z. Chen).

0272-8842/$ - see front matter © 2013 Elsevier Ltd and Techna Group S.r.l. All rights reserved.
http://dx.doi.org/10.1016/j.ceramint.2013.10.052

metastable N_2 and ozone photo-induced dissociation can assist the removal of organic residues [47]. The bandgaps of sol–gel derived $Mg_xZn_{1-x}O$ thin films are successfully engineered from ~3.25 to ~3.50 eV by varying Mg content up to 20%. The films show good transparency in the visible light wavelength region. APPJ treatment increases the top-layer grain connectivity, slightly sharpens the absorption edges, and reduces the bandgaps. APPJ is a good candidate for a rapid thermal annealing process.

2. Experimental procedures

The $Mg_xZn_{1-x}O$ sol–gel solution was prepared by dissolving zinc acetate dihydrate ($Zn(CH_3COO)_2 \cdot 2H_2O$, ≥98%, Sigma-Aldrich) and magnesium acetate tetrahydrate ($Mg(CH_3COO)_2 \cdot 4H_2O$, ≥98%, J.T. Baker) in isopropyl alcohol. Monoethanolamine (C_2H_7NO, MEA, ≥99%, Sigma-Aldrich) was used as a stabilizer. The molar ratio of MEA to the total ion concentration was maintained at 1. The Mg content x ($x = [Mg^{2+}]/([Zn^{2+}]+[Mg^{2+}])$) was varied as 0, 0.05, 0.1, and 0.2 respectively; the total ion concentration was fixed at 0.3 M. Then, the mixture was stirred at 70 °C for 3 h to form a clear homogeneous solution. After the stirring process, the transparent solution was aged for 24 h at room temperature. Finally, the sol–gel solution was filtered using a 0.45-μm filter.

The filtered solution was spin-coated onto 2 cm × 2 cm Corning Eagle-2000 glass substrates at 3000 rpm for 30 s. This coating process was repeated five times for the film to reach ~200 nm thickness, which was measured using a profilometer (KLA-Tencor Alpha Step 500). After each coating step, a 10-min, 300 °C thermal process was performed on a hotplate. APPJ was then used to anneal the resultant $Mg_xZn_{1-x}O$ thin films. The schematic of the APPJ apparatus used in this study is shown in Fig. 1. The plasma jet consists of stainless-steel, cylindrical-type electrodes with the inner and outer electrodes being powered and grounded, respectively [48]. The diameters of the inner and outer electrodes are 1.5 and 3.5 cm, respectively. A pulsed power source supplied dc pulse voltage up to 350 V with a repetitive frequency up to 25 kHz, followed by a transformer that increases the voltage of up to 21 kV. The plasmas underwent glow to arc transition within each power period. Such an arrangement sustained a jet of high reactivity and great power controllability [49,50]. The dc pulse voltage was the control parameter of the plasma jet. A quartz tube of 2-cm length was installed at the downstream of the plasma jet to confine the convective flow and to minimize the influence of ambient air [51]. The applied conditions for APPJ surface treatment were: applied voltage, 275 V; air (79% N_2 +21% O_2, 99.995%) flow rate, 35 slm; on/off duty cycle, 7/33 μs; and 1-mm gap between the quartz tube exit and the platform. The surface temperature evolution upon the exposure to the APPJ was monitored using a K-type thermocouple. The temporal evolution of the temperature was acquired using a data acquisition device (USB-6221, National Instruments) and recorded using a computer. Fig. 2 shows the temperature evolution for the APPJ surface treatment process. From 0 to 30 s, the temperature increases rapidly, following which the temperature increases slowly and becomes steady. The temperatures of the substrate at various times are tabulated in Table 1. The highest surface temperature was ~630 °C.

We determined the stoichiometric composition of the sol–gel derived $Mg_xZn_{1-x}O$ films by using an electron probe X-ray microanalyzer (EPMA, JEOL JXA-8200) (in this particular experiment, the sol–gel derived $Mg_xZn_{1-x}O$ films were deposited on a p-Si (100) wafer). Three measurements were taken on each sample; the detected positions were 2 mm apart. The crystalline structure of the APPJ-annealed $Mg_xZn_{1-x}O$ films was examined by X-ray diffraction (PANlytical X'Pert Pro). The morphology was investigated using a scanning electron microscope (SEM, Nova™ NanoSEM 230). The transmittance was measured by a UV–vis spectrophotometer

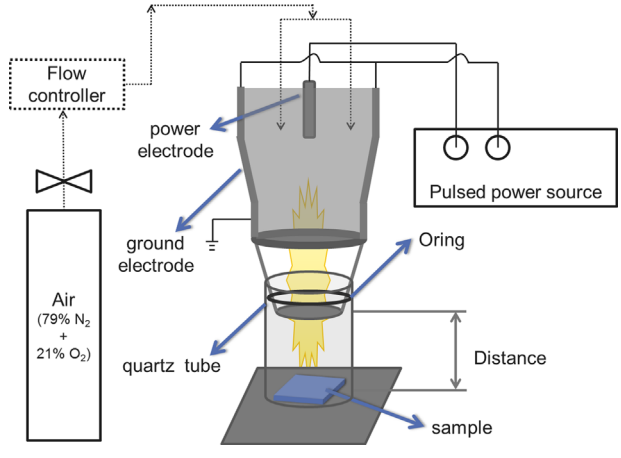

Fig. 1. The schematic of atmospheric pressure plasma jet (APPJ) apparatus.

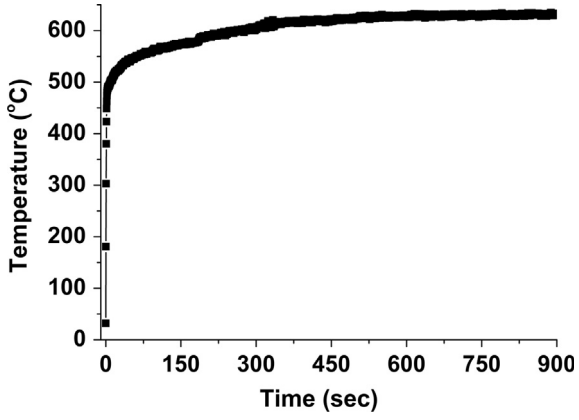

Fig. 2. Evolution of the substrate surface temperature during the APPJ surface treatment process.

Table 1
The approximate temperatures at various times.

Annealed time (min)	Temp. (°C)
1	550
5	600
10	630
15	632

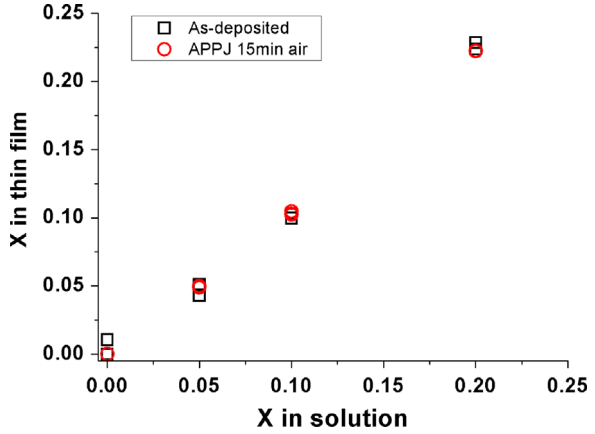

Fig. 3. Mg composition in $Mg_xZn_{1-x}O$ thin films made by various starting solutions.

(Jasco V-670). For measuring the resistivity, a 100-nm-thick titanium layer was deposited upon the $Mg_xZn_{1-x}O$ films by an e-beam evaporator and then patterned as coplanar electrical contacts. The resistivity was evaluated using an electrometer (Keitheley 2636A).

3. Results and discussion

The stoichiometric composition of the sol–gel derived $Mg_xZn_{1-x}O$ films was determined by EPMA. All EPMA data of the $Mg_xZn_{1-x}O$ films are in fair agreement with the compositions of the starting sol–gel solutions, as shown in Fig. 3. The composition remains almost the same after APPJ treatment. Fig. 4 shows the XRD patterns of $Mg_xZn_{1-x}O$ thin films. The sharp peak at ~34° is attributed to wurtzite (002).

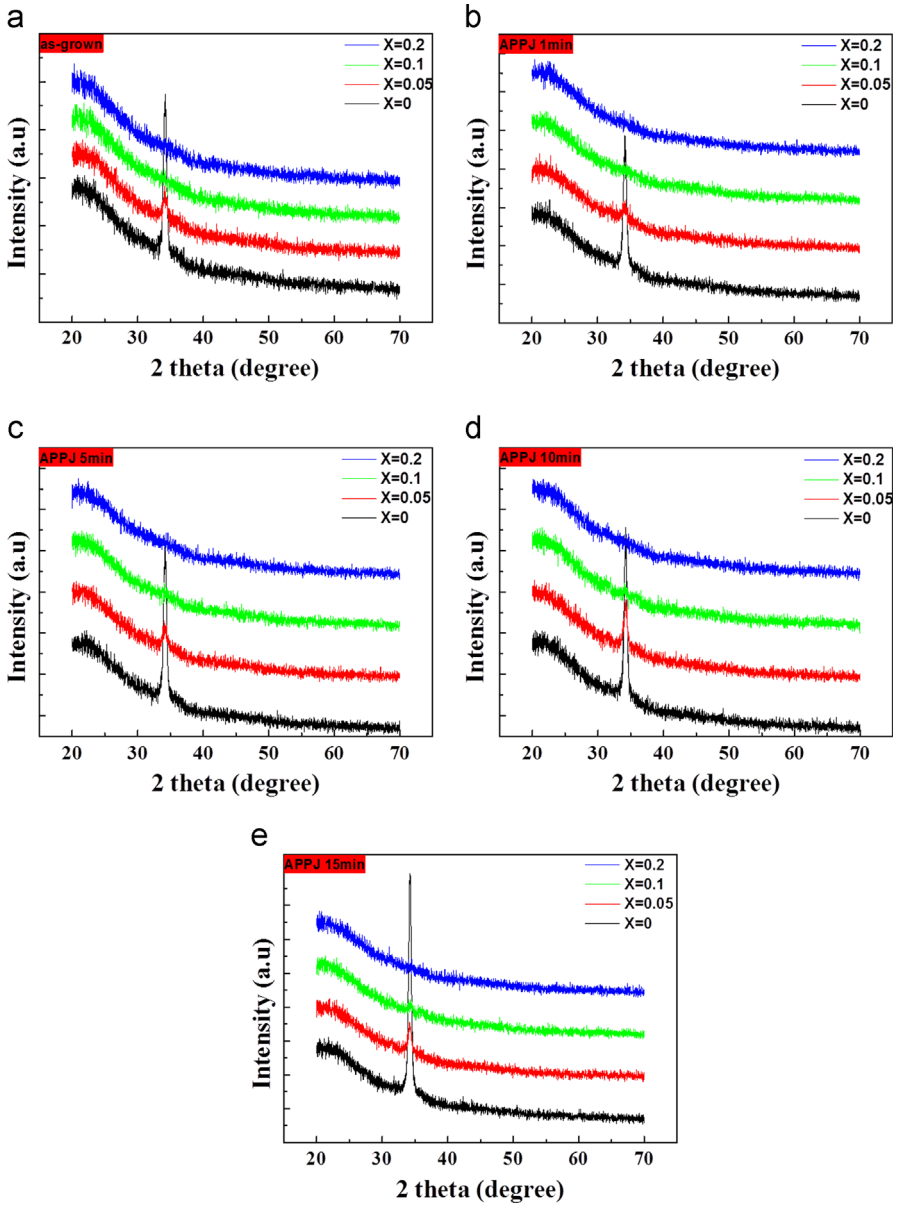

Fig. 4. XRD patterns of $Mg_xZn_{1-x}O$ thin films preheated at 300 °C for 10 min, followed by APPJ-treatment of various durations: (a) as-grown (only 10 min, 300 °C preheating), (b) 1 min, (c) 5 min, (d) 10 min and (e) 15 min.

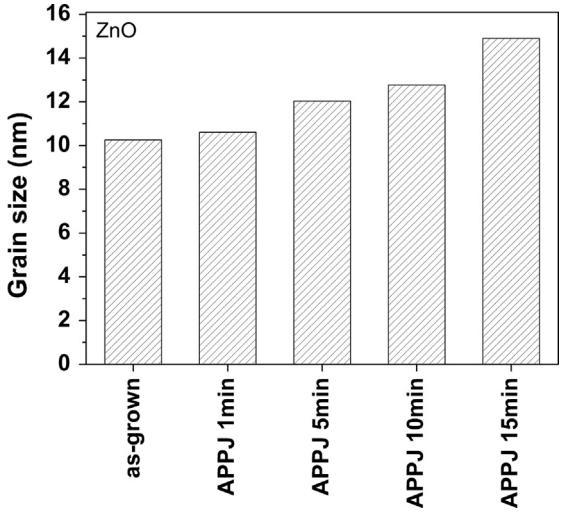

Fig. 5. Calculated grain size of APPJ annealed ZnO films using Scherrer's equation.

The deposited films with $x \leq 0.05$ reveal a strong (002) preferential orientation. As the APPJ annealing time is further increased, the relative intensity of the (002) diffraction peak increases with narrowed full-width-at-half-maximum (FWHM). The average grain size of the ZnO film is estimated using Scherrer's formula [52,53].

$$D = \left(\frac{0.9\lambda}{W \cos \theta}\right) \quad (1)$$

where λ is the X-ray wavelength (λ=0.154 nm for Cu-Kα) and W is the FWHM in radians. The calculated average grain sizes are plotted in Fig. 5. The crystal size of as-grown (only 300 °C preheating, no APPJ treatment) film is ~10 nm. The grain size increases with the APPJ-annealing time. These results indicate that the APPJ annealing process can increase the crystallinity and grain size. The average grain size of $Mg_xZn_{1-x}O$ films is not identified because the intensity of the diffraction peaks is too weak to accurately estimate the FWHM. The crystallinity

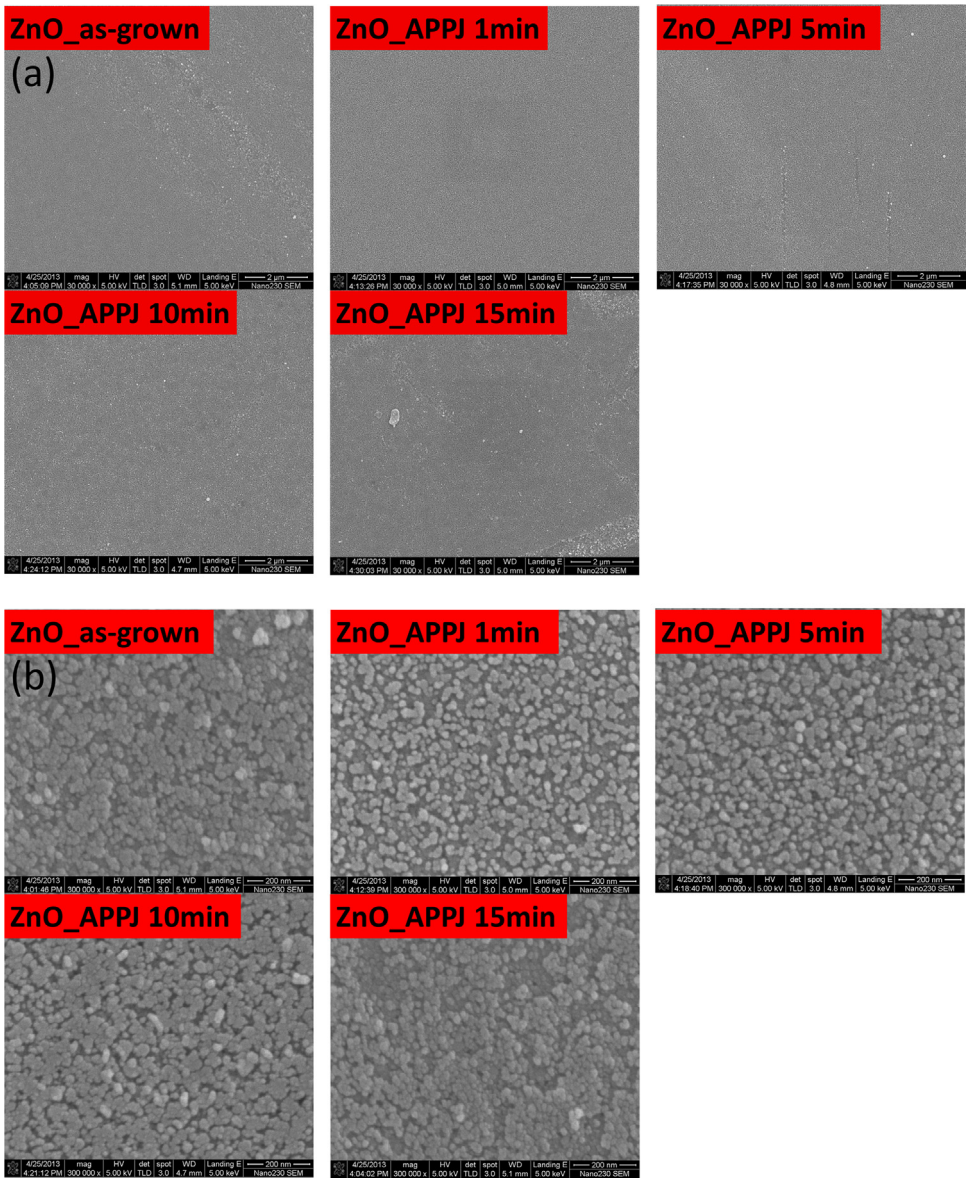

Fig. 6. SEM images for ZnO (x=0) thin films annealed by APPJs: (a) 30,000× and (b) 300,000×.

generally degrades with the addition of Mg to ZnO. For high Mg content films ($x \geq 0.1$), the (002) diffraction peak becomes very small such that the effect of APPJ treatment on the crystallinity is difficult to identify by XRD patterns.

SEM images of the as-grown and APPJ-annealed ZnO films are shown in Fig. 6. Fig. 6(a) and (b) shows 30,000 × and 300,000 × magnifications, respectively. Under 30,000 × magnification, the sol–gel derived ZnO films appear to be very smooth. Under 300,000 × magnification (Fig. 6(b)), the as-grown and APPJ-annealed films exhibit grainy features. APPJ annealing does not significantly alter the surface morphology. Nevertheless, the grains become more connected when the APPJ annealing time exceeds 10 min. This is similar to the results of our previous study of a rf-sputtered ZnO film [29]. The top layer of the film is sintered by the highly reactive plasmas. SEM images of the $Mg_{0.2}Zn_{0.8}O$ films are shown in Fig. 7. Under 30,000 × magnification, some wrinkles are observed on the sol–gel derived $Mg_{0.2}Zn_{0.8}O$ films. Compressive stresses caused by the difference in the thermal expansion coefficients between the film and the substrate are generated during the drying process, leading to the wrinkling of the sol–gel-derived thin films [54]. The wrinkles smoothen as the APPJ annealing time increases, probably owing to the sintering effect and the stress relaxation in the films.

The optical transmittance spectra of the sol–gel derived $Mg_xZn_{1-x}O$ films are shown in Fig. 8. The average optical transmittances of the films are greater than 80% in the visible wavelength range of 400–800 nm. The absorption edge of the $Mg_xZn_{1-x}O$ films shifts toward a shorter wavelength as the Mg content increases from 0% to 20% in all cases. Moreover, the absorption edges of the as-grown $Mg_xZn_{1-x}O$ films are much less sharp than those of films annealed by APPJs. The absorption edges of APPJ-annealed $Mg_xZn_{1-x}O$ films become sharper with an increase in the APPJ annealing time. This should be related to

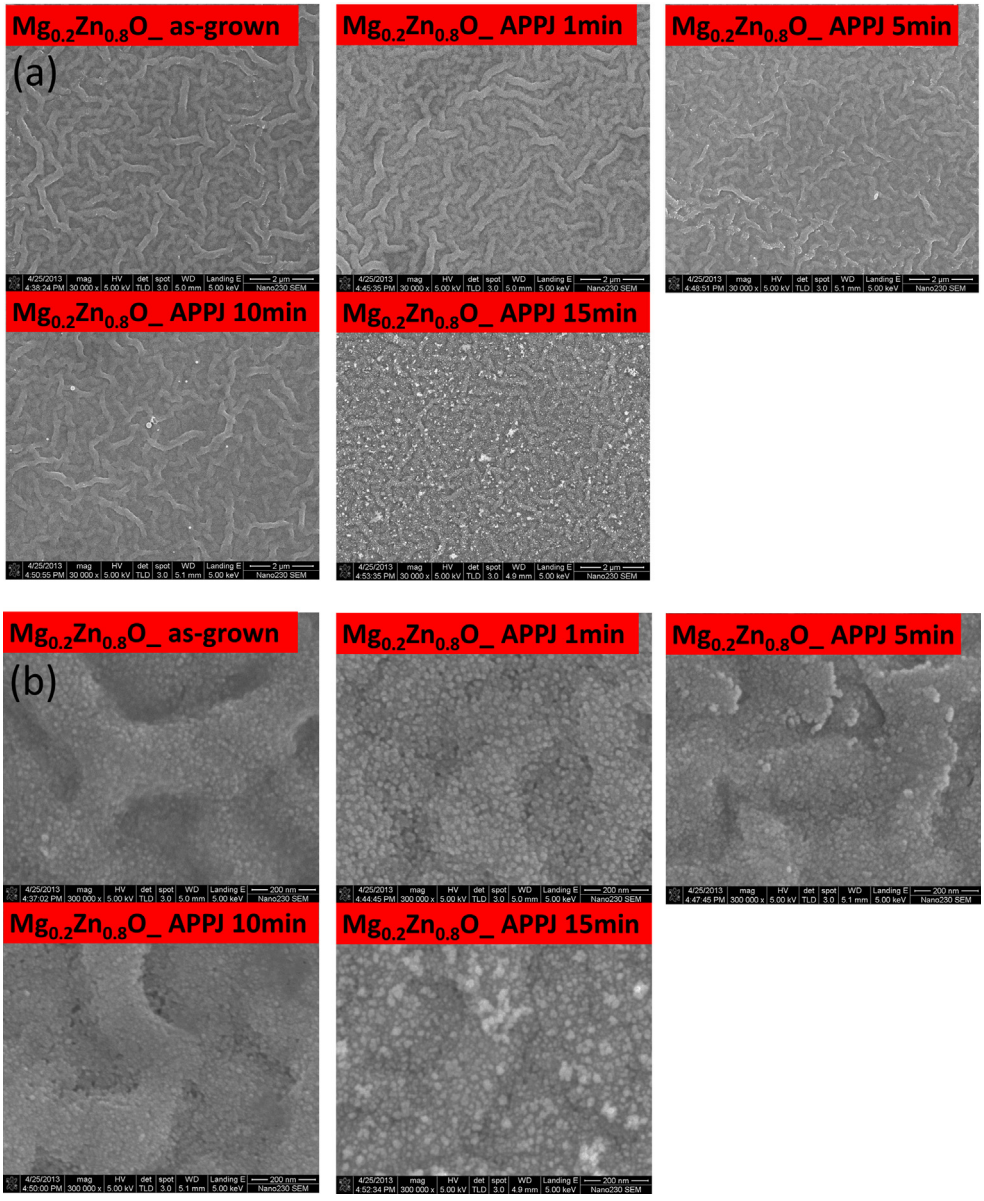

Fig. 7. SEM images of $Mg_{0.2}Zn_{0.8}O$ thin films annealed by APPJs: (a) 30,000 × and (b) 300,000 × .

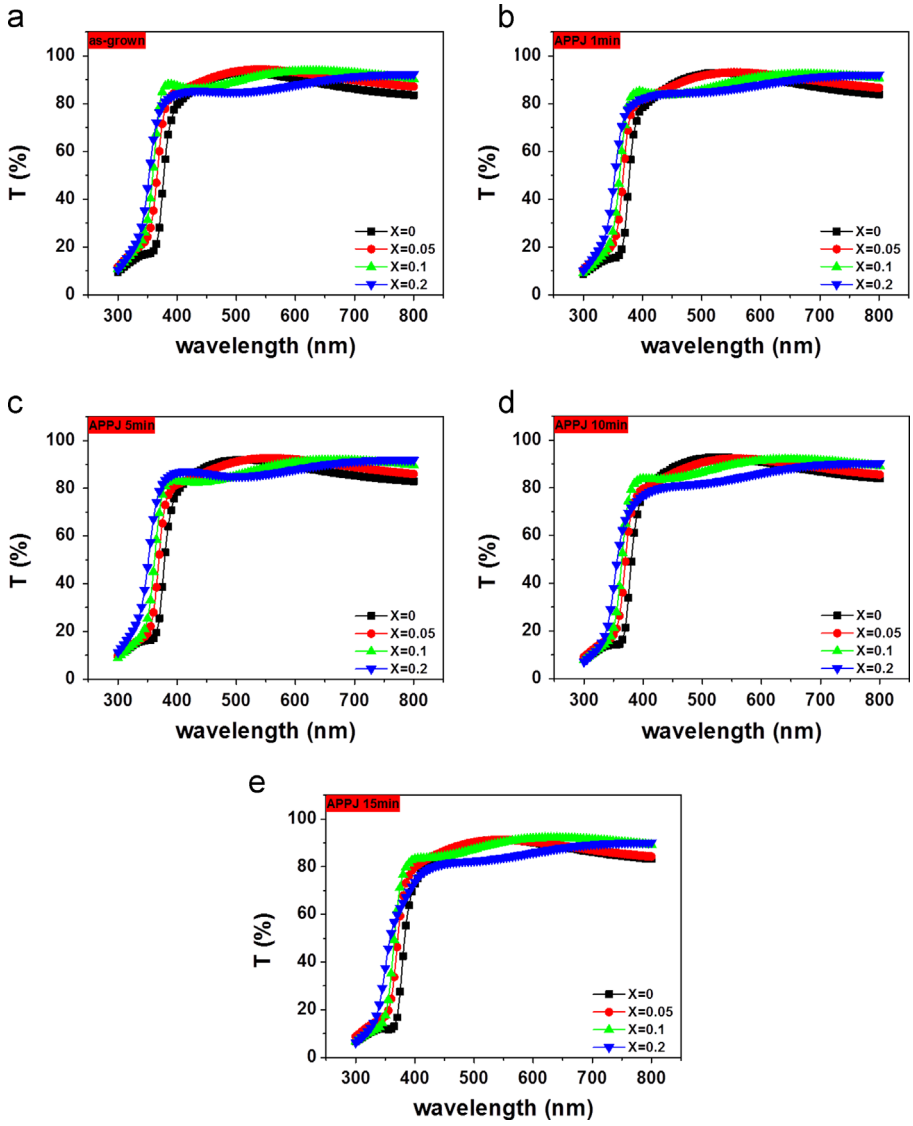

Fig. 8. Optical transmission spectra of $Mg_xZn_{1-x}O$ thin films annealed by APPJs with various durations: (a) as-grown, (b) 1 min, (c) 5 min (d) 10 min, and (e) 15 min.

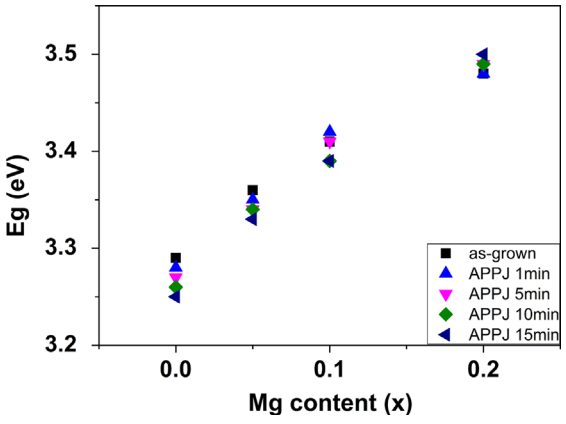

Fig. 9. Optical bandgaps of $Mg_xZn_{1-x}O$ thin films annealed by APPJs.

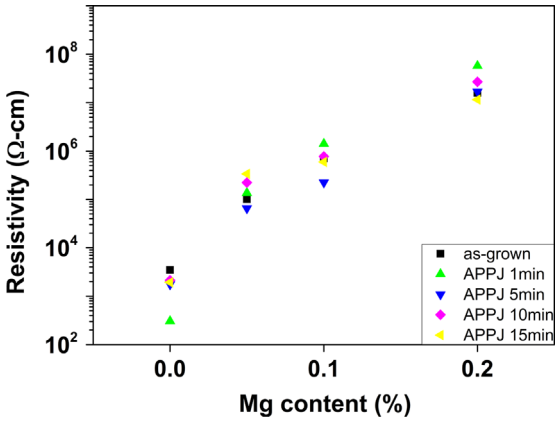

Fig. 10. Resistivity of $Mg_xZn_{1-x}O$ thin films annealed by APPJs.

the crystallinity. Because the films contain nanoscale grains, the quantum confinement effect becomes significant. In nanoscale grains, the bandgap is slightly modified by the grain size [21,55–57]

$$E_{g,nanocrystal} = E_{g,bulk} + \frac{\pi^2\hbar^2}{2R^2}\left(\frac{1}{m_e^*} + \frac{1}{m_h^*}\right) - 0.248E_{Ry} \quad (2)$$

where $E_{g,nanocrystal}$ and $E_{g,bulk}$ are the bandgaps for the nanocrystalline film and the bulk material, respectively. E_{Ry} is the exciton binding energy; R is the grain radius; and m_e^* and m_h^* are the effective masses of the electrons and the holes, respectively. As described previously, the APPJ treatment may slightly increase the grain size, leading to slight bandgap narrowing and absorption edge slope alteration. The optical bandgap can be determined by the Tauc equation [58]

$$(\alpha h\upsilon)^n = A(h\upsilon - E_g) \quad (3)$$

where A is a constant; $h\upsilon$ is the photon energy; E_g is the optical bandgap; α is the absorption coefficient; and $n=2$ for the direct bandgap. The calculated bandgaps are shown in Fig. 9. The bandgap increases with the Mg content in the alloyed films, indicating that Mg atoms are incorporated into the ZnO crystal lattice sites [42]. The bandgap is successfully tailored from ~3.25 to ~3.5 eV by varying the Mg content up to 20%. Generally, the bandgap decreases with the APPJ annealing time. The trend of bandgap reduction is most obvious for ZnO and $Mg_{0.05}Zn_{0.95}O$ and becomes unclear for films with higher Mg contents, probably owing to the severe degradation of crystallinity. This agrees with the prediction by Eq. (2). When the films are amorphous or nanocrystalline, the grain boundary quantum confinement becomes significant. Therefore, the optical bandgap becomes slightly smaller after APPJ treatment, owing to the slight increase in grain size [55–57]. The electrical resistivity of $Mg_xZn_{1-x}O$ thin films with various Mg contents is shown in Fig. 10. The resistivity of $Mg_xZn_{1-x}O$ thin films increases with the Mg content, which is attributed to the widening of the optical bandgap when more Mg is substituted for Zn in the lattice sites. The increased bandgap results in less thermally excited carriers in the conduction bands, leading to a decrease in the conductivity [4,7,18]. The stronger bonding strength of Mg–O than Zn–O (the fractional ionic character is 0.61 for ZnO and 0.84 for MgO) makes Mg a good suppressor of oxygen vacancies [59,60]. This could also lead to an increase in resistivity as Mg is added to the ZnO film.

4. Conclusions

Sol–gel derived nanocrystalline $Mg_xZn_{1-x}O$ thin films ($0.2 \geq x \geq 0$) annealed by APPJs were investigated. The optical bandgap of APPJ-annealed $Mg_xZn_{1-x}O$ thin films was successfully tailored from ~3.25 to ~3.50 eV by varying the Mg content. The absorption band edge became sharper as the APPJ treatment time increased, which was attributed to the slight grain growth in the films. Owing to the quantum confinement effects in amorphous/nanocrystalline materials, the bandgap generally decreased with the increase in grain size caused by the APPJ treatment. Some wrinkle features, caused by the built-in stresses during solvent evaporation, were observed in $Mg_{0.2}Zn_{0.8}O$ thin films. Highly energetic APPJs sintered the top layer of the films, thereby increasing the connectivity of grains. Nevertheless, the resistivity was not significantly changed by APPJ treatment for 15 min. In comparison to ZnO, the resistivity of $Mg_{0.2}Zn_{0.8}O$ thin films increased by three to four orders of magnitude.

Acknowledgments

This work is supported by the National Science Council of Taiwan, under Grant nos. NSC 102-2221-E-002-060, NSC 100-2221-E-002-151-MY3, and NSC 101-2628-E-002-020-MY3. The authors would like to thank Mr. Chung-Yuan Kao of Instrumentation Center of National Taiwan University for his assistance with the EPMA operation.

References

[1] U. Ozgur, Y.I. Alivov, C. Liu, A. Teke, M.A. Reshchikov, S. Dogan, V. Avrutin, S.J. Cho, H. Morkoc, A comprehensive review of ZnO materials and devices, J. Appl. Phys. 98 (4) (2005) 041301.
[2] M.W. Ahn, K.S. Park, J.H. Heo, J.G. Park, D.W. Kim, K.J. Choi, J.H. Lee, S.H. Hong, Gas sensing properties of defect-controlled ZnO-nanowire gas sensor, Appl. Phys. Lett. 93 (26) (2008) 263103.
[3] L.J. Bie, X.N. Yan, J. Yin, Y.Q. Duan, Z.H. Yuan, Nanopillar ZnO gas sensor for hydrogen and ethanol, Sens. Actuat B – Chem. 126 (2) (2007) 604–608.
[4] Y.-S. Tsai, J.-Z. Chen, Positive gate-bias temperature stability of rf-sputtered $Mg_xZn_{1-x}O$ active-layer thin-film transistors, IEEE Trans. Electron Devices 59 (1) (2012) 151–158.
[5] C.H. Li, Y.S. Tsai, J.Z. Chen, Negative bias temperature instability of Rf-sputtered $Mg_{0.05}Zn_{0.95}O$ thin film transistors with MgO gate dielectrics, Semicond. Sci. Technol. 26 (10) (2011) 105007.
[6] E.M.C. Fortunato, P.M.C. Barquinha, A.C.M.B.G. Pimentel, A.M.F. Goncalves, A.J.S. Marques, L.M.N. Pereira, R.F.P. Martins, Fully transparent ZnO thin-film transistor produced at room temperature, Adv. Mater. 17 (5) (2005) 590.
[7] G.H. Kim, W.H. Jeong, B. Du Ahn, H.S. Shin, H.J. Kim, H.J. Kim, M.K. Ryu, K.B. Park, J.B. Seon, S.Y. Lee, Investigation of the effects of Mg incorporation into InZnO for high-performance and high-stability solution-processed thin film transistors, Appl. Phys. Lett. 96 (16) (2010) 163506.
[8] Y.S. Tsai, C.H. Li, I.C. Chiu, H.A. Chin, I.C. Cheng, J.Z. Chen, Effects of drain-bias and ambient on hump formation in the transfer curves of positively gate-biased MgZnO thin film transistors, Thin Solid Films 529 (2013) 360–363.
[9] Y. Choi, K. Lee, C.H. Park, K.H. Lee, J.W. Nam, M.M. Sung, K.M. Lee, H.C. Sohn, S. Im, High current fast switching n-ZnO/p-Si diode, J. Phys. D: Appl. Phys. 43 (34) (2010) 345101.
[10] M. Cavas, R.K. Gupta, A.A. Al-Ghamdi, O.A. Al-Hartomy, F. El-Tantawy, F. Yakuphanoglu, Fabrication and electrical characterization of transparent NiO/ZnO p–n junction by the sol–gel spin coating method, J. Sol–Gel Sci. Technol. 64 (1) (2012) 219–223.
[11] J.Z. Zhao, H.W. Liang, J.C. Sun, J.M. Bian, Q.J. Feng, L.Z. Hu, H.Q. Zhang, X.P. Liang, Y.M. Luo, G.T. Du, Electroluminescence from n-ZnO/p-ZnO:Sb homojunction light emitting diode on sapphire substrate with metal-organic precursors doped p-type ZnO layer grown by MOCVD technology, J. Phys. D: Appl. Phys. 41 (19) (2008) 195110.
[12] C.T. Chi, I.C. Cheng, J.Z. Chen, Bandgap tuning of MgZnO in flexible transparent $n^{(+)}$-ZnO:Al/n-MgZnO/p-$CuAlO_x$:Ca diodes on polyethylene terephthalate substrates, J. Alloys Compd. 544 (2012) 111–114.
[13] C.T. Chi, I.F. Lu, I.C. Chiu, P.Y. Chen, B.W. Huang, I.C. Cheng, J.Z. Chen, Flexible transparent ZnO:Al/ZnO/$CuAlO_{(x)}$:Ca heterojunction diodes on polyethylene terephthalate substrates, J. Electron. Mater. 42 (6) (2013) 1242–1245.
[14] X.H. Xie, Z.Z. Zhang, B.H. Li, S.P. Wang, M.M. Jiang, C.X. Shan, D.X. Zhao, H.Y. Chen, D.Z. Shen, Mott-type $Mg_xZn_{1-x}O$-based visible-blind ultraviolet photodetectors with active anti-reflection layer, Appl. Phys. Lett. 102 (23) (2013) 231122.
[15] Y.N. Hou, Z.X. Mei, H.L. Liang, D.Q. Ye, C.Z. Gu, X.L. Du, Dual-band MgZnO ultraviolet photodetector integrated with Si, Appl. Phys. Lett. 102 (15) (2013) 153510.

[16] S. Han, Z.Z. Zhang, J.Y. Zhang, L.K. Wang, J. Zheng, H.F. Zhao, Y.C. Zhang, M.M. Jiang, S.P. Wang, D.X. Zhao, C.X. Shan, B.H. Li, D.Z. Shen, Photoconductive gain in solar-blind ultraviolet photodetector based on $Mg_{0.52}Zn_{0.48}O$ thin film, Appl. Phys. Lett. 99 (24) (2011) 242105.
[17] D. Schmid, M. Ruckh, H.W. Schock, A comprehensive characterization of the interfaces in Mo/CIS/CdS/ZnO solar cell structures, Sol. Energy Mater. Sol. Cells 41–42 (0) (1996) 281–294.
[18] J.Z. Chen, C.H. Li, I.C. Cheng, Phase transitions of room temperature RF-sputtered $ZnO/Mg_{0.4}Zn_{0.6}O$ multilayer thin films after thermal annealing, Thin Solid Films 520 (6) (2012) 1918–1923.
[19] E.Y. Jung, S.G. Lee, S.H. Sohn, D.K. Lee, H.K. Kim, Electrical properties of plasma display panel with $Mg_{1-x}Zn_xO$ protecting thin films deposited by a radio frequency magnetron sputtering method, Appl. Phys. Lett. 86 (15) (2005) 153503.
[20] A. Ohtomo, M. Kawasaki, T. Koida, K. Masubuchi, H. Koinuma, Y. Sakurai, Y. Yoshida, T. Yasuda, Y. Segawa, $Mg_xZn_{1-x}O$ as a II–VI widegap semiconductor alloy, Appl. Phys. Lett. 72 (19) (1998) 2466–2468.
[21] S.T. Tan, B.J. Chen, X.W. Sun, W.J. Fan, H.S. Kwok, X.H. Zhang, S.J. Chua, Blueshift of optical band gap in ZnO thin films grown by metal-organic chemical-vapor deposition, J. Appl. Phys. 98 (1) (2005) 013505.
[22] J.F. Chien, Y.H. Huang, Y.J. Chang, J.J. Shyue, J.R. Yang, M. Shiojiri, M.J. Chen, Tunable optical and structural properties of $Mg_xZn_{1-x}O$ films prepared by in situ atomic layer doping technique, ECS J. Solid State Sci. 2 (1) (2013) P31–P35.
[23] H.J. Lee, J.A. Lee, J.H. Lee, Y.W. Heo, J.J. Kim, S.K. Park, J. Lim, Optical band gap modulation by Mg-doping in $In_2O_3(ZnO)_{(3)}$ ceramics, Ceram. Int. 38 (8) (2012) 6693–6697.
[24] G.H. Kim, W.H. Jeong, B. Du Ahn, H.S. Shin, H.J. Kim, H.J. Kim, M.K. Ryu, K.B. Park, J.B. Seon, S.Y. Lee, Investigation of the effects of Mg incorporation into InZnO for high-performance and high-stability solution-processed thin film transistors, Appl. Phys. Lett. 96 (16) (2010) 163506.
[25] H. Tampo, H. Shibata, K. Matsubara, A. Yamada, P. Fons, S. Niki, M. Yamagata, H. Kanie, Two-dimensional electron gas in Zn polar ZnMgO/ZnO heterostructures grown by radical source molecular beam epitaxy, Appl. Phys. Lett. 89 (13) (2006) 132113.
[26] M. Yano, K. Hashimoto, K. Fujimoto, K. Koike, S. Sasa, M. Inoue, Y. Uetsuji, T. Ohnishi, K. Inaba, Polarization-induced two-dimensional electron gas at $Zn_{1-x}Mg_xO$/ZnO heterointerface, J. Cryst. Growth 301–302 (0) (2007) 353–357.
[27] H.A. Chin, I.C. Cheng, C.I. Huang, Y.R. Wu, W.S. Lu, W.L. Lee, J.Z. Chen, K.C. Chiu, T.S. Lin, Two dimensional electron gases in polycrystalline MgZnO/ZnO heterostructures grown by rf-sputtering process, J. Appl. Phys. 108 (5) (2010) 054503.
[28] H.A. Chin, I.C. Cheng, C.K. Li, Y.R. Wu, J.Z. Chen, W.S. Lu, W.L. Lee, Electrical properties of modulation-doped rf-sputtered polycrystalline MgZnO/ZnO heterostructures, J. Phys. D: Appl. Phys. 44 (45) (2011) 455101.
[29] S.-T. Lien, H.-C. Li, Y.-J. Yang, C.-C. Hsu, I.-C. Cheng, J.-Z. Chen, Atmospheric pressure plasma jet annealed ZnO films for MgZnO/ZnO heterojunctions, J. Phys. D: Appl. Phys. 46 (7) (2013) 075202.
[30] C.I. Huang, H.A. Chin, Y.R. Wu, I.C. Cheng, J.Z. Chen, K.C. Chiu, T. S. Lin, Mobility enhancement of polycrystalline MgZnO/ZnO thin film layers with modulation doping and polarization effects, IEEE Trans. Electron Dev. 57 (3) (2010) 696–703.
[31] A. Tsukazaki, S. Akasaka, K. Nakahara, Y. Ohno, H. Ohno, D. Maryenko, A. Ohtomo, M. Kawasaki, Observation of the fractional quantum Hall effect in an oxide, Nat. Mater. 9 (11) (2010) 889–893.
[32] M. Nakano, A. Tsukazaki, A. Ohtomo, K. Ueno, S. Akasaka, H. Yuji, K. Nakahara, T. Fukumura, M. Kawasaki, Electronic-field control of two-dimensional electrons in polymer-gated-oxide semiconductor heterostructures, Adv. Mater. 22 (8) (2010) 876.
[33] I.C. Cheng, B.S. Wang, H.H. Hou, J.Z. Chen, MgZnO/ZnO heterostructure field-effect transistors fabricated by rf-sputtering, ECS Trans. 50 (8) (2013) 83–93.
[34] S. Fujita, H. Tanaka, S. Fujita, MBE growth of wide band gap wurtzite MgZnO quasi-alloys with MgO/ZnO superlattices for deep ultraviolet optical functions, J. Cryst. Growth 278 (1–4) (2005) 264–267.
[35] J.W. Dong, A. Osinsky, B. Hertog, A.M. Dabiran, P.P. Chow, Y.W. Heo, D.P. Norton, S.J. Pearton, Development of MgZnO–ZnO–AlGaN heterostructures for ultraviolet light emitting applications, J. Electron. Mater. 34 (4) (2005) 416–423.
[36] S. Heitsch, G. Benndorf, G. Zimmermann, C. Schulz, D. Spemann, H. Hochmuth, H. Schmidt, T. Nobis, M. Lorenz, M. Grundmann, Optical and structural properties of MgZnO/ZnO hetero- and double heterostructures grown by pulsed laser deposition, Appl. Phys. A – Mater. 88 (1) (2007) 99–104.
[37] C. Bundesmann, M. Schubert, A. Rahm, D. Spemann, H. Hochmuth, M. Lorenz, M. Grundmann, Infrared dielectric function and phonon modes of Mg-rich cubic $Mg_xZn_{1-x}O$ ($x \geq 0.67$) thin films on sapphire (0001), Appl. Phys. Lett. 85 (6) (2004) 905.
[38] D. Xin, L. Yanbo, H. Keke, Z. Wang, Y. Yin, X. Xiaochuan, Z. Yuantao, W. Jin, Z. Baolin, D. Guotong, Study on the p-MgZnO/i-ZnO/n-MgZnO light-emitting diode fabricated by MOCVD, J. Phys. D: Appl. Phys. 42 (23) (2009) 235101.
[39] L.K. Wang, Z.G. Ju, C.X. Shan, J. Zheng, D.Z. Shen, B. Yao, D.X. Zhao, Z.Z. Zhang, B.H. Li, J.Y. Zhang, MgZnO metal–semiconductor–metal structured solar-blind photodetector with fast response, Solid State Commun. 149 (45–46) (2009) 2021–2023.
[40] S. Han, D.Z. Shen, J.Y. Zhang, Y.M. Zhao, D.Y. Jiang, Z.G. Ju, D.X. Zhao, B. Yao, Characteristics of cubic MgZnO thin films grown by radio frequency reaction magnetron co-sputtering, J. Alloys Compd. 485 (1-2) (2009) 794–797.
[41] S.R. Meher, K.P. Biju, M.K. Jain, Effect of post-annealing on the band gap of sol–gel prepared nano-crystalline $Mg_xZn_{1-x}O$ ($0.0 \leq x \leq 0.3$) thin films, J. Sol–Gel Sci. Technol. 52 (2) (2009) 228–234.
[42] M. Wang, E.J. Kim, S. Kim, J.S. Chung, I.-K. Yoo, E.W. Shin, S.H. Hahn, C. Park, Optical and structural properties of sol–gel prepared MgZnO alloy thin films, Thin Solid Films 516 (6) (2008) 1124–1129.
[43] S. Suwanboon, P. Amornpitoksuk, P. Bangrak, N. Muensit, Optical, photocatalytic and bactericidal properties of $Zn_{1-x}La_xO$ and $Zn_{1-x}Mg_xO$ nanostructures prepared by a sol–gel method, Ceram. Int. 39 (5) (2013) 5597–5608.
[44] M. Sahal, B. Marí, M. Mollar, F.J. Manjón, $Zn_{1-x}Mg_xO$ thin films deposited by spray pyrolysis, Phys. Status Solidi C 7 (9) (2010) 2306–2310.
[45] X. Zhang, X.M. Li, T.L. Chen, J.M. Bian, C.Y. Zhang, Structural and optical properties of $Zn_{1-x}Mg_xO$ thin films deposited by ultrasonic spray pyrolysis, Thin Solid Films 492 (1–2) (2005) 248–252.
[46] H. Chang, Y.-J. Yang, H.-C. Li, C.-C. Hsu, I. Cheng, J.-Z. Chen, Preparation of nanoporous TiO_2 films for DSSC application by a rapid atmospheric pressure plasma jet sintering process, J. Power Sources 234 (2013) 16–22.
[47] M.-H. Chiang, K.-C. Liao, I.-M. Lin, C.-C. Lu, H.-Y. Huang, C.-L. Kuo, J.-S. Wu, C.-C. Hsu, S.-H. Chen, Effects of oxygen addition and treating distance on surface cleaning of ITO glass by a non-equilibrium nitrogen atmospheric-pressure plasma jet, Plasma Chem. Plasma Process. 30 (5) (2010) 553–563.
[48] Y.W. Hsu, H.C. Li, Y.J. Yang, C.C. Hsu, Deposition of zinc oxide thin films by an atmospheric pressure plasma jet, Thin Solid Films 519 (10) (2011) 3095–3099.
[49] Y.W. Hsu, Y.J. Yang, C.Y. Wu, C.C. Hsu, Downstream characterization of an atmospheric pressure pulsed arc jet, Plasma Chem. Plasma Process. 30 (3) (2010) 363–372.
[50] C.-C. Hsu, C.-Y. Wu, Electrical characterization of the glow-to-arc transition of an atmospheric pressure pulsed arc jet, J. Phys. D: Appl. Phys. 42 (21) (2009) 215202.
[51] C.-C. Hsu, Y.-J. Yang, The increase of the jet size of an atmospheric-pressure plasma jet by ambient air control, IEEE Trans. Plasma Sci. 38 (3) (2010) 496–499.
[52] A.L. Patterson, The Scherrer formula for X-ray particle size determination, Phys. Rev. 56 (10) (1939) 978–982.
[53] P. Scherrer, Estimation of the size and internal structure of colloidal particles by means of röntgen, vol. 2, Nachrichten von der Akademie der Wissenschaften, Gottingen, 1918, p. 98.

[54] S.J. Kwon, J.H. Park, J.G. Park, Wrinkling of a sol–gel-derived thin film, Phys. Rev. E: Stat., Nonlinear, Soft Matter Phys. 71 (1 Pt. 1) (2005) 011604.
[55] S. Mandal, R.K. Singha, A. Dhar, S.K. Ray, Optical and structural characteristics of ZnO thin films grown by rf magnetron sputtering, Mater. Res. Bull. 43 (2) (2008) 244–250.
[56] Y. Kayanuma, Quantum-size effects of interacting electrons and holes in semiconductor microcrystals with spherical shape, Phys. Rev. B: Condens. Matter 38 (14) (1988) 9797–9805.
[57] I. Kosacki, V. Petrovsky, H.U. Anderson, Band gap energy in nanocrystalline ZrO_2:16% Y thin films, Appl. Phys. Lett. 74 (3) (1999) 341.
[58] J. Tauc, in: J. Tauc (Ed.), Amorphous and Liquid Semiconductors, Plenum, 1974.
[59] A. Onodera, N. Tamaki, K. Jin, H. Yamashita, Ferroelectric properties in piezoelectric semiconductor $Zn_{1-x}M_xO$ (M=Li, Mg), Jpn. J. Appl. Phys. Part 1 36 (9B) (1997) 6008–6011.
[60] Y. Ogawa, S. Fujihara, Band-gap modification and tunable blue luminescence of wurtzite $Mg_xZn_{1-x}O$ thin films, Phys. Status Solidi A 202 (9) (2005) 1825–1828.